Tracking the nuclear-wave-packet dynamics on excited bound states of Ar_2^+ in strong laser fields

Menghang Shi,[1,*] Chenxu Lu,[1,*] Shengzhe Pan,[1] Lianrong Zhou,[1] Hongcheng Ni,[1] Peifen Lu,[1] Wenbin Zhang,[1,†] and Jian Wu[1,2,‡]

[1]*State Key Laboratory of Precision Spectroscopy, East China Normal University, Shanghai 200241, China*

[2]*Chongqing Key Laboratory of Precision Optics, Chongqing Institute of East China Normal University, Chongqing 401121, China; Collaborative Innovation Center of Extreme Optics, Shanxi University, Taiyuan, Shanxi 030006, China; and CAS Center for Excellence in Ultra-intense Laser Science, Shanghai 201800, China*

(Received 19 June 2023; accepted 21 September 2023; published 9 October 2023)

We experimentally investigated the photoionization and fragmentation of a van der Waals cluster of argon dimer (Ar_2) exposed to intense laser fields. By performing femtosecond pump-probe experiments in a reaction microscope, we tracked the spatiotemporal evolution of the nuclear wave packet (NWP) launching onto the excited bound states of Ar_2^+. By interrogating the measured time-resolved vibrational structures in the kinetic energy spectra obtained from Coulomb explosion imaging of the Ar_2^+ NWP, the vibrational revival and rotational excitation of the long-living rovibrational NWP were observed in real time. The vibrational populations of the NWP on the potential curves of three excited bound states of Ar_2^+, i.e., $I(3/2)_g$, $II(1/2)_u$, and $I(3/2)_u$, were identified by the Fourier analysis of the time-dependent kinetic energy spectra of nuclear fragments.

DOI: 10.1103/PhysRevA.108.043108

I. INTRODUCTION

Direct imaging of the light-induced nuclear wave packet (NWP) of molecules could greatly improve our understanding of the quantum dynamics of nuclear motion in the photochemical reactions. A powerful tool for tracking the ultrafast NWP motion in light-driven molecules is suggested by combining the femtosecond pump-probe arrangement with the Coulomb explosion imaging technique [1,2]. In such approach, the pump pulse prepares a bound or dissociating NWP by ionizing or exciting the molecule, and the probe pulse projects the NWP wave function onto the Coulomb repulsive state. The NWP dynamics can then be revealed by monitoring the time-resolved kinematic emission of the repelling nuclear fragments. Using such scheme, the spatiotemporal evolution of rotational, vibrational, and dissociation motion of the NWP has been observed in covalent diatomic molecules, such as H_2 [3–5], D_2 [6–8], N_2 [9,10], O_2 [11,12], and CO [10,13].

As compared to the covalently bound molecules, the noble gas dimers are bound by weak van der Waals (vdW) forces. The large internuclear distance of the vdW dimers gives rise to the localization of electrons at the two atomic centers. This makes the NWP dynamics differ from that of strongly bound molecules [14–16]. For instance, due to the shallow potential wells of the noble gas dimer and their cations, the vibrational periods of the populated bound NWP are longer than those of covalent molecules by an order of magnitude. The feature of relatively slow nuclear motion has made the noble gas dimer ions suitable for investigating the vibrational echo phenomena in a single molecule [17]. Moreover, due to their simple electronic structure and large internuclear distance, the noble gas dimers have widely been used to study the intermolecular charge transfer reactions [18,19]. The time-resolved NWP dynamics of the rare-gas dimer and their cations, which is important for understanding the strong-field intersystem interaction, however, has received comparatively less attention to date.

The argon dimer (Ar_2) is a prototypical vdW molecule. As motivated by the importance in development of rare-gas laser technology [20,21], its singly ionized state Ar_2^+ has been studied extensively both theoretically [22] and experimentally [23]. Due to its simple electronic structure, Ar_2^+ is also considered as a clean model system for studying the properties of large rare-gas cluster ions [24,25]. *Ab initio* quantum chemical calculations [26] and spectroscopic experiments [27] have shown that Ar_2^+ possesses six low-lying and closely spaced electronic states [see Fig. 1(b)], labeled as $I(1/2)_u$, $I(1/2)_g$, $I(3/2)_u$, $I(3/2)_g$, $II(1/2)_u$, and $II(1/2)_g$ [28–30], where I and II designate electronic states correlating to the two dissociation limits of Ar_2^+, and g, u are the electronic parities. The nuclear vibrational and rotational properties on various states have been mostly investigated in spectroscopic study [27]. Ion coincidence measurements have enabled the study of laser-induced dissociation dynamics of the bound NWP populating on the lowest and deepest state $I(1/2)_u$ of Ar_2^+ [31,32]. Yet, to the best of our knowledge, the spatiotemporal imaging of the laser-induced dynamics of the bound NWP on the other electronic states of Ar_2^+ with a relatively shallower well has still not been thoroughly experimentally explored.

In this paper, we experimentally studied the rovibrational motion of the Ar_2^+ NWP on the $I(3/2)_g$, $II(1/2)_u$, and $I(3/2)_u$ states. The spatiotemporal evolution of the NWP is imaged by using a femtosecond pump-probe approach with

*These authors contributed equally to this work.
†wbzhang@lps.ecnu.edu.cn
‡jwu@phy.ecnu.edu.cn

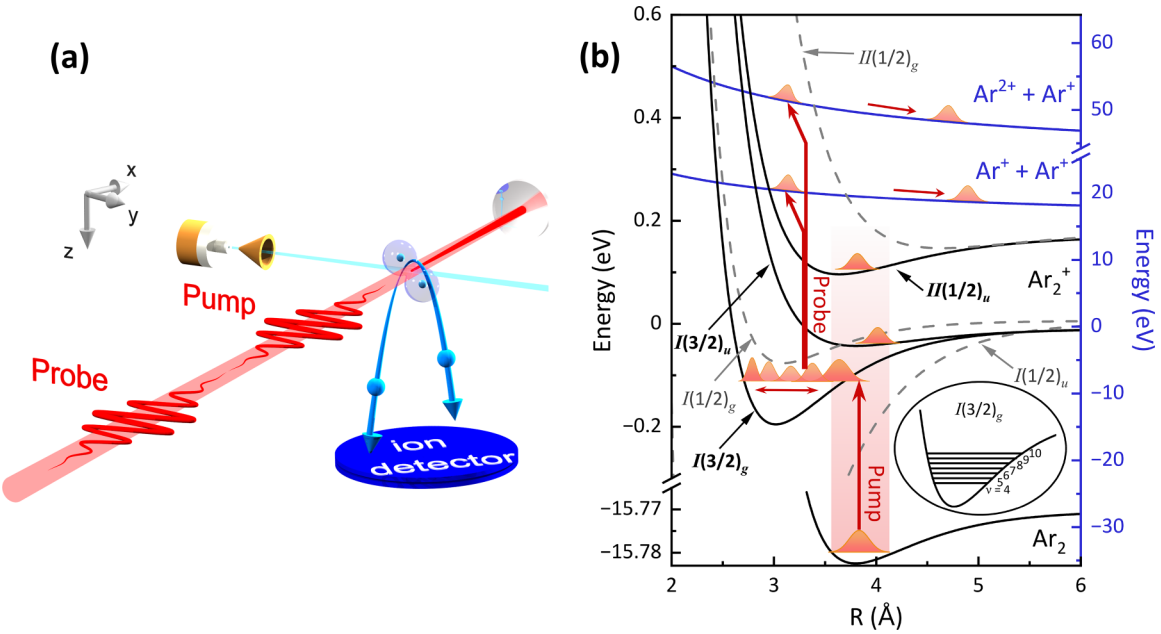

FIG. 1. (a) Schematic diagram of the experimental setup. (b) Illustration of the potential energy curves relevant for the pump-probe approach in the experiment. The potential energy curves of the ground state of neutral Ar_2 and the six low-lying electronic states of Ar_2^+ are depicted in the left vertical coordinates in black. The blue curves in the right vertical coordinate show the two Coulomb repulsive states, $Ar^+ + Ar^+$ and $Ar^{2+} + Ar^+$, respectively. For the Ar_2^+ states, the potential curves of the $I(3/2)_g$, $II(1/2)_u$, and $I(3/2)_u$ states studied in this work are represented by the solid black lines, while that of the other three states are plotted using dashed gray lines. Initially, the Ar_2 dimer at the equilibrium internuclear distance $R_{eq} \sim 3.8$ Å is singly ionized by the pump pulse, followed by the population of vibrational NWPs onto Ar_2^+ bound states of $I(3/2)_g$, $II(1/2)_u$, and $I(3/2)_u$ via a Franck-Condon vertical transition. For the sake of simplicity, only the motions of the NWPs on the $I(3/2)_g$ state of Ar_2^+ are depicted for illustration. A time-delayed probe pulse is used to either induce the two-site double or triple ionization followed by Coulomb-exploded fragmentation into $Ar^+ + Ar^+$ or $Ar^{2+} + Ar^+$. The inset illustrates the vibrational levels of the nuclear wave packets propagating on the Ar_2^+ $I(3/2)_g$ state. The six potential energy curves of Ar_2^+ are adapted from Ref. [30].

the Coulomb explosion imaging technique. As depicted in Fig. 1(b), an intense pump pulse ionizes the neutral Ar_2 and launches bound NWPs onto the Ar_2^+ states. As induced by a delayed probe pulse, the long-living Ar_2^+ NWPs may undergo further ionization towards the Coulomb repulsive states, where the NWP finally dissociates into two ionic fragments repelling each other. By coincidently measuring the time-resolved kinetic energy release (KER) spectra of the resulting nuclear fragment pairs from the Coulomb explosion channels, we tracked the NWP motion of Ar_2^+ in real time. The rovibrational NWP dynamics on different bound states of Ar_2^+ were revealed by the Fourier analysis of the observed time-dependent oscillating structures. The long-term (up to ~400 ps) field-free evolution allows us to resolve the collapse and fractional revival of the Ar_2^+ NWP.

II. EXPERIMENTAL METHODS

As schematically shown in Fig. 1(a), the experimental measurements were performed in a reaction microscope of cold target recoil-ion momentum spectroscopy (COLTRIMS) [33,34]. Details on the setup can be found in Refs. [35,36]. Neutral Ar_2 molecules were produced through a collimated supersonic jet of Ar gas with a driving pressure of 2.4 bars. The detailed geometry of the jet system and the parameters of the supersonic expansion source, such as the driving pressure and gas source temperature, ensure that a fraction of about 1% Ar_2 dimers are produced with respect to the atomic Ar monomer in the jet beam [37–39], and the density of the Ar_2 dimers in the laser focal volume is estimated to be 3.2×10^6 particles/cm^3. A linearly polarized femtosecond laser pulse derived from a multipass amplifier Ti:sapphire laser system (28 fs, 790 nm, 10 kHz) was fed through a Mach-Zehnder interferometer to produce pump and probe pulses. The time delay between the two pulses was finely adjusted with a step size of 40 fs using a motorized stage. The laser pulses were later recombined and tightly focused onto the supersonic molecular beam by using a concave silver mirror ($f = 7.5$ cm) inside the vacuum chamber. The intensity of the pump and probe pulses at the interaction region was estimated to be $\sim3.5\times10^{14}$ and $\sim3.0\times10^{14}$ W/cm^2, respectively. The KER spectra and three-dimensional (3D) momentum distribution of the laser-created charged fragments were reconstructed from their time of flight and positions recorded using a time- and position-sensitive detector.

III. RESULTS AND DISCUSSION

To conduct the Coulomb explosion imaging method, we concentrated on the Coulomb-exploded $Ar_2(1, 1)$ and $Ar_2(2, 1)$ channels, where the neutral Ar_2 finally breaks into $Ar^+ + Ar^+$, and $Ar^{2+} + Ar^+$, respectively. The two ionic fragments in each channel are detected in coincidence by considering the momentum conservation law. In the experiments, the ion yield rates for the $Ar_2(1, 1)$ and $Ar_2(2, 1)$ channels are estimated to be 24.8×10^{-3} (events/laser shot) and 4.72×10^{-3}

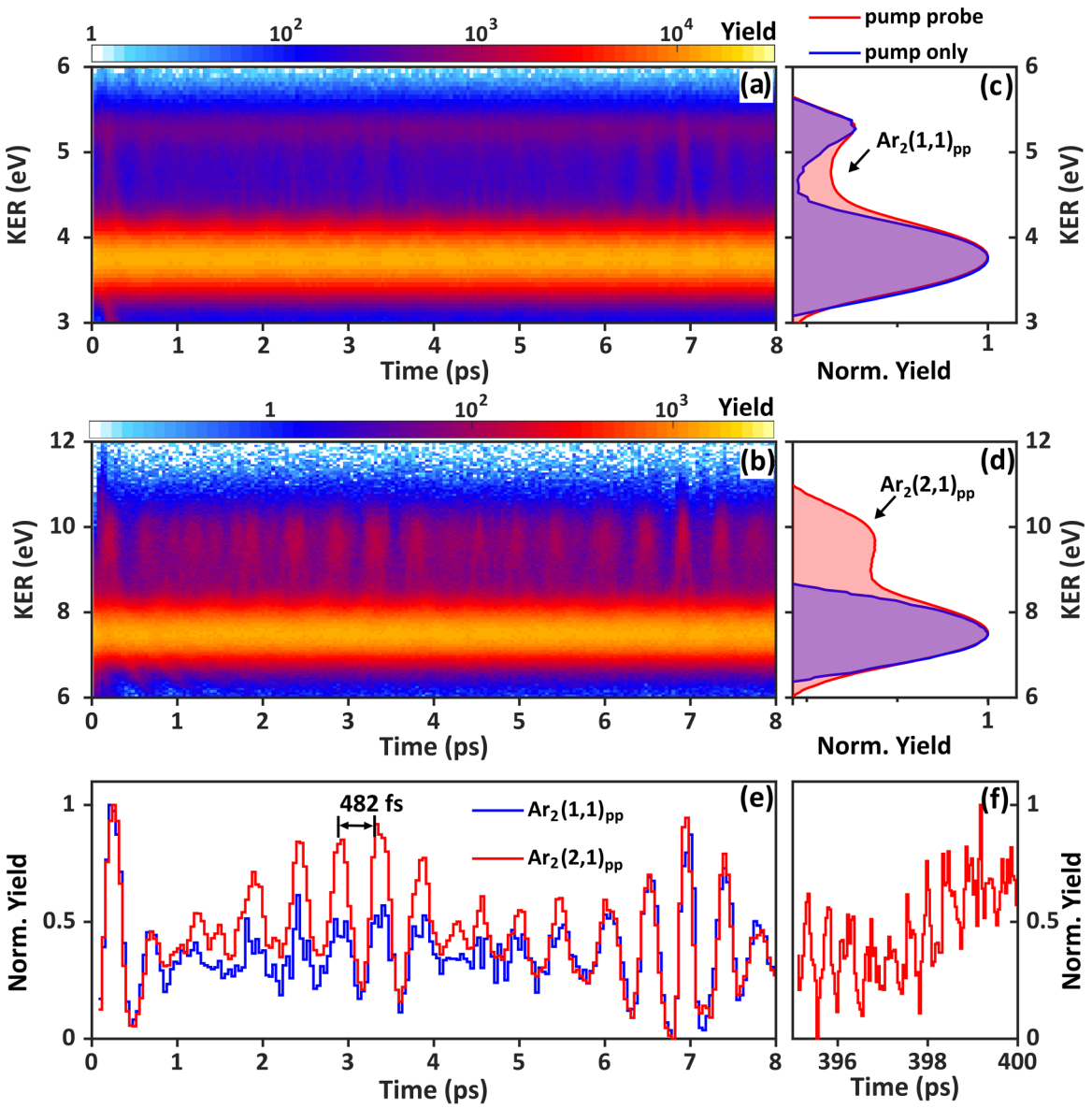

FIG. 2. (a), (b) Measured time-dependent nuclear KER spectra of fragmentation channels of (a) $Ar_2(1, 1)$ and (b) $Ar_2(2, 1)$. (c), (d) Time-integrated KER distributions of fragmentation channels of (c) $Ar_2(1, 1)$ and (d) $Ar_2(2, 1)$ measured with the pump-probe scheme (red curve) and pump only (blue curve). (e) The time-dependent ion yields of the $Ar_2(1, 1)_{pp}$ channel (blue curve) and the $Ar_2(2, 1)_{pp}$ channel (red curve) obtained by integrating over the KER range from 4.5 to 5 eV in (a) and the KER range from 8.5 to 11 eV in (b). (f) Measured KER-integrated (8.5 eV$<$ KER $<$ 11 eV) ion yields of the $Ar_2(2, 1)_{pp}$ channel for time delay ranging from 395 to 400 ps.

(events/laser shot), respectively. Figures 2(a) and 2(b) show the measured KER spectra of the $Ar_2(1, 1)$ and $Ar_2(2, 1)$ channels, respectively, as a function of the time delay between the pump and probe pulses. The ion yields of the dominant KER band lying at ∼3.8 eV for the $Ar_2(1, 1)$ channel, and ∼7.5 eV for the $Ar_2(2, 1)$ channel, are essentially delay independent. As shown in Figs. 2(c) and 2(d), the two main KER peaks in the corresponding time-integrated KER spectra are comparable with that obtained using only the pump pulse. These two peaks stem from the direct two-site double and triple ionization of neutral Ar_2, respectively, followed by Coulomb-exploded fragmentation at equilibrium internuclear distance of $R_{eq} \sim 3.8$ Å [38]. Besides the main peak, a minor peak with higher KER at 5.3 eV can be observed in the KER spectra of the $Ar_2(1, 1)$ channel. This 5.3 eV peak is attributed to a relaxation process involving spontaneous radiative charge transfer [40], which can be induced by the femtosecond pump or probe pulses individually.

Clear time-dependent ion yield distributions with broad and periodic stripes are observed in the KER region with 3.8 eV $<$ KER $<$ 5.3 eV for the $Ar_2(1, 1)$ channel, and the KER region with KER $>$ 7.5 eV for the $Ar_2(2, 1)$ channel. As shown in Figs. 2(c) and 2(d), the corresponding time-integrated ion yields exhibit noticeably enhanced distribution in the KER spectra as compared to that measured with a single pump pulse. This indicates that the signals emerged in the KER spectra of the $Ar_2(1, 1)$ and $Ar_2(2, 1)$ channels, labeled as $Ar_2(1, 1)_{pp}$ and $Ar_2(2, 1)_{pp}$, respectively, originate from the collaborated contributions by the pump and probe pulses.

The observed pump-probe-induced periodic stripes in Figs. 2(a) and 2(b) can be attributed to the following processes. As illustrated in Fig. 1(b), the pump pulse initially releases an electron from one site of the neutral Ar_2. After the single ionization, a vibrational NWP composed by a number of vibrational states is created on the Ar_2^+ bound state of $I(3/2)_g$ or $II(1/2)_u$ or $I(3/2)_u$ via Franck-Condon vertical transition. The bound NWP classically propagates inwards and outwards on the potential energy curves, which may also undergo dispersion due to the anharmonicity of the Ar_2^+ potential curves. To visualize time-dependent dynamics of the bound NWP, it is crucial to introduce a time delayed probe pulse to further ionize the Ar_2^+ ion and project the propagating NWP onto the Coulomb repulsive curve, exploding the molecular ion. The single or double ionization of Ar_2^+ induced by the probe pulse leads to the $Ar_2(1, 1)_{pp}$ and $Ar_2(2, 1)_{pp}$ channels, respectively. By scanning the time delay between the pump and probe pulses, the dynamics of a bound NWP on the Ar_2^+ states can thus be encoded into the time-resolved ion yields of the Coulomb explosion channels. In analogy to the previous pump-probe studies for the covalent molecules [4,6,7,9–11], the measurements of time-resolved oscillation of a bound-state NWP allow one to track the spatiotemporal evolution of the NWP on the Ar_2^+ intermediate state.

Figure 2(e) shows the KER-integrated oscillating yields for the $Ar_2(1, 1)_{pp}$ (blue curve) and $Ar_2(2, 1)_{pp}$(red curve) channels. For the two curves, the well-matched oscillation periodic structures with nearly identical oscillation period suggest that the bound NWPs populated onto the Ar_2^+ state towards the $Ar_2(1, 1)_{pp}$ and $Ar_2(2, 1)_{pp}$ channels have comparable vibrational dynamics in the time domain. We note that the phase shift between the oscillation structures, if they exist—which might be caused by the ultrashort time delay between the formation process of the $Ar_2(1, 1)_{pp}$ and $Ar_2(2, 1)_{pp}$ channels—is hard to distinguish in the presented results due to the large step size of the pump-probe scan. By inspecting the oscillating structures, the fast collapse dynamics of the vibrational NWP and its subsequent revival on Ar_2^+ state are observed. Because of the anharmonicity of the Ar_2^+ potential curve, the vibrational levels populated by the pump pulse are not equally spaced in potential energy. Therefore, the propagation of NWP on the potential curve will undergo diffusion instead of regular oscillation after a few oscillations [6,7]. This is reflected in the apparent decaying oscillation amplitude of the vibrational structures for delay around 1 and 5 ps, as shown in Fig. 2(e). After about 7 ps, comparable strong oscillating structures reappear, indicating restored periodicity of the vibrational NWP motion [13]. This is attributed to the quantum vibrational revival of the NWP, where the propagating NWP will later return back to its initial position after a field-free evolution [41–43]. With the vibrational revival time of the Ar_2^+ NWP being ∼14 ps, the here-observed reappearance of oscillations corresponds to half revival [17]. As shown in Fig. 2(f), in spite of the dissipation of coherent vibration motion, the coherence of vibrational structures is well preserved even at a large time delay of ∼400 ps, indicating a rather long lifetime of the vibrational NWP on the involved states of Ar_2^+.

We also visualized the spatial evolution of the NWP on the Ar_2^+ state in real time by exploiting the Coulomb explosion imaging [44]. Considering that the bound Ar_2^+ NWP is nearly at rest with negligible kinetic energy at the instant of explosion, the internuclear distance R of the Ar_2^+ ion can be directly reconstructed from the measured KER using the Coulomb law. Figure 3(a) shows the differentially normalized NWP probability density of the $Ar_2(2, 1)_{pp}$ channel as a function of the internuclear distance R and the pump-probe time delay. To increase the visibility and eliminate the time-independent signal induced by an individual pump or probe pulse, a background subtraction is employed in this two-dimensional (2D) map. Note that similar R- and time-resolved oscillating structures are observed for the $Ar_2(1, 1)_{pp}$ channel as well, indicating comparable NWP dynamics for both channels in the spatial domain. In Fig. 3(a), the fast-ascending tilted line structures propagating beyond $R \sim 4.0$ Å within less than 1 ps are originated from the pump-pulse-induced direct dissociation of the Ar_2^+ NWP, which is Coulomb explosion imaged by the probe pulse. The broad oscillating structures spreading between $R \sim 2.7$ Å and $R \sim 4$ Å reflect the back-and-forth stretching motion of the vibrational NWPs on the Ar_2^+ bound state.

The observed characteristic oscillation structures also enable one to identify the major states contributing to the bound-state NWP motion of the Ar_2^+ ion. The oscillation period of the observed oscillating structures is ∼482 fs, which is longer than the previously studied vibrational period (∼250 fs) of the Ar_2^+ ion in the lowest $I(1/2)_u$ state [31,32]. This indicates that higher electronic states of Ar_2^+ with a relatively shallower potential well are populated. The oscillatory structures are a consequence of the quantum beating of coherently superposed wave functions at various vibrational levels on the bound states [6]. To quantitatively reveal the vibrational states contributing to the oscillating structures and identify the involved electronic states in the nuclear dynamics of Ar_2^+, we studied the vibrational structures in the frequency domain by a Fourier analysis of its time evolution trace [3]. The time-dependent ion yields of the $Ar_2(2, 1)_{pp}$ channel as a function of internuclear distance R shown in Fig. 3(a) were Fourier transformed to resolve the contributing vibrational transitions' coherence ($\nu_{i-1} \rightarrow \nu_i$), where i is the vibrational quantum number. In order to achieve higher resolution, the time-delay range was extended up to 47 ps. The obtained 2D power spectrum of R versus frequency is shown in Fig. 3(b). The distribution is dominated by three R-resolved regions with frequencies in the ranges 1000–1200 GHz, 1500–1700 GHz, and 1900–2800 GHz, which implies population of bound NWPs on various states of Ar_2^+.

The Fourier transformed intensity spectra integrating over different R ranges are shown in Figs. 3(c)–3(e). Each peak represents a transition coherence between the adjacent vibrational states. There are two dominant peaks in the intensity spectra with 4.0 Å $< R <$ 4.5 Å, and 3.2 Å $< R <$ 3.5 Å, respectively, and multiple peaks in the intensity spectra with 2.5 Å $< R <$ 3.2 Å. The corresponding transition frequencies $f(\nu_{i-1} \rightarrow \nu_i)$ of the spectral peaks are listed in Table I. By matching the frequencies of the vibrational transitions obtained in the experiments with that known from the

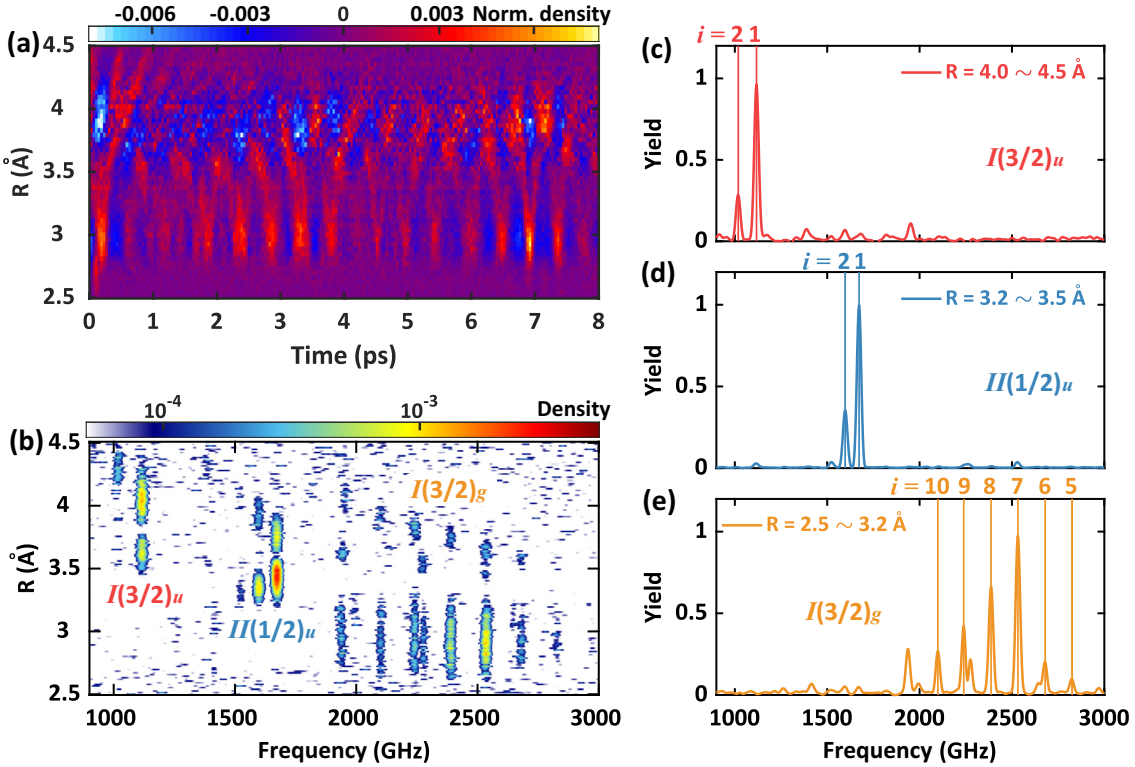

FIG. 3. (a) The differentially normalized density distribution of the Ar_2^+ NWP as a function of the internuclear distance R and the pump-probe delay. The R distributions are reconstructed from the experimental data of the $Ar_2(2, 1)_{pp}$ channel according to the Coulomb law of KER $= 2/R$. The background subtraction is applied to the 2D map of KER versus time to eliminate the time-independent signal from an individual pump or probe pulse. (b) The 2D Fourier transform frequency spectra for the R versus time spectrum of the $Ar_2(2, 1)$ channel measured with time delay scanning from 0 to 47 ps. (c)–(e) R-integrated 1D frequency spectra with different R ranges: 4.0–4.5 Å, 3.2–3.5 Å, and 2.5–3.2 Å, respectively. The vibrational transitions ($\nu_{i-1} \rightarrow \nu_i$) in the different Ar_2^+ states are indicated by the colored vertical lines.

spectroscopic data of various states of Ar_2^+ [30], the observed two dominant spectral peaks in Figs. 3(c) and 3(d) are identified to be mostly contributed from the vibrational transitions of $\nu_0 \rightarrow \nu_1$, $\nu_1 \rightarrow \nu_2$ on the $I(3/2)_u$ and $II(1/2)_u$ states of Ar_2^+, respectively. The electronic state responsible for the various spectral peaks in Fig. 3(e) for 2.5 Å $< R <$ 3.2 Å is identified to be the $I(3/2)_g$ state of Ar_2^+, where several frequency peaks are assigned to the adjacent vibrational transitions between ν_5 and ν_{10}. Moreover, we also inspected the potential energy parameters for the three different states

TABLE I. Comparison of the experimental results with the spectroscopic data in the literature [27,30]. For the vibrational transition coherence frequency $f(\nu_{i-1} \rightarrow \nu_i)$, the experimental values were obtained from the Fourier analysis of the experimental data, while the referenced values were derived from the calculation of the energy differences of the vibrational energy levels of the corresponding electronic states in Ref. [30]. The frequency unit of cm^{-1} in [30] has been converted to GHz using the relation 1 cm^{-1} = 29.979 25 GHz. For the potential energy parameters of vibrational constant ω_e, and anharmonicity constant $\omega_e x_e$, the referenced values for the $I(3/2)_u$, $II(1/2)_u$, and $I(3/2)_g$ states of Ar_2^+ are obtained from Ref. [27].

		$f(\nu_{i-1} \rightarrow \nu_i)$ (GHz)		ω_e (cm^{-1})		$\omega_e x_e$ (cm^{-1})	
State	i	Expt.	Ref. [30]	Expt.	Ref. [27]	Expt.	Ref. [27]
$I(3/2)_u$	1	1116.7	1121.2	40.5	41.7	1.64	1.90
	2	1018.3	1022.3				
$II(1/2)_u$	1	1672.3	1678.8	58.3	58.6	1.26	1.30
	2	1597.0	1600.9				
$I(3/2)_g$	5	2823.0	2857.0	117.9	118	2.45	2.49
	6	2678.9	2689.1				
	7	2531.6	2521.2				
	8	2386.9	2374.3				
	9	2238.6	2257.4				
	10	2098.5	2188.5				

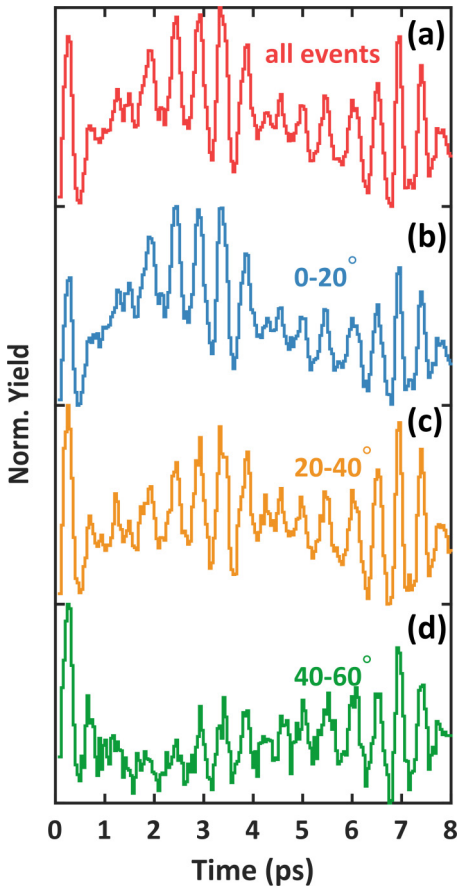

FIG. 4. (a)–(d) Measured normalized ion yields in the $Ar_2(2, 1)_{pp}$ channel in the yz plane as a function of the pump-probe time delay, integrating over (a) all ion emission angles θ (b) $0^\circ \leqslant \theta \leqslant 20^\circ$, (c) $20^\circ \leqslant \theta \leqslant 40^\circ$, and (d) $40^\circ \leqslant \theta \leqslant 60^\circ$, relative to the laser polarization direction.

of Ar_2^+. The frequency $f(\nu_{i-1} \rightarrow \nu_i)$ of vibrational transition coherence between the levels ν_{i-1} and ν_i is given by $f(\nu_{i-1} \rightarrow \nu_i) = \omega_e - 2\omega_e x_e i$, where i is the vibrational quantum number, ω_e is the vibrational constant, and $\omega_e x_e$ is the anharmonicity constant [43]. As shown in Table I, for the involved three states, the characteristic parameters, ω_e and $\omega_e x_e$, obtained from the experimental data are in good agreement with the values reported in the previous spectroscopic study [27]. This further confirms our assignment of the three excited bound states of $I(3/2)_u$, $II(1/2)_u$, and $I(3/2)_g$ of Ar_2^+ contributing to the observed vibrational NWP dynamics. Here we directly visualize the coherent vibrational motions of the NWPs on these states in real time.

Finally, we turn our attention to the rotation dynamics of the NWP on the Ar_2^+ state. In Fig. 2(e), it can be observed that the initially degenerated vibrational structures yield a significant enhancement around 3.5 ps before the occurrence of vibrational revival (half revival) at around 7 ps. The enhanced yield of the vibrational structures around 3.5 ps is caused by the postpulse field-free alignment of the Ar_2^+ NWP induced by the pump pulse. The dynamical NWP alignment is probed by the later-arriving probe pulse by tracing the subsequent fragmentation of the aligned molecular ion [39]. The excitation of rotational NWPs in the Ar_2^+ states can be confirmed by inspecting the Coulomb explosion rate for various angular intervals $\Delta\theta$ of the exploding molecule with respect to the laser polarization. Here the θ is defined as the ion emission angle in the laser polarization plane (yz plane), and $\theta = 0^\circ$ indicates a molecular fragmentation along the laser polarization direction (y axis). Taking the vibrational structures in the $Ar_2(2, 1)_{pp}$ channel as an example, the corresponding fragmentation yield integrated over all θ is shown in Fig. 4(a) for comparison. As shown in Figs. 4(b)–4(d), significant differences among the spectra with varying $\Delta\theta$ can be observed around 3.5 ps. The ion yields at ~3.5 ps for $\Delta\theta_1 = 0^\circ$–20° are significantly enhanced as compared to that for larger $\Delta\theta$. For $\Delta\theta_1 = 40^\circ$–$60^\circ$ in Fig. 4(d), a suppressed envelope of the overall vibrational structure can be observed, showing a trend of antialignment of the molecular ion. This clearly indicates that the dynamical alignment of the Ar_2^+ NWP is induced by the y-polarized pump pulse. Moreover, as shown in Fig. 2(e), the $Ar_2(2, 1)_{pp}$ channel shows a stronger response of the impulsive alignment than that of the $Ar_2(1, 1)_{pp}$ channel. This is in line with the expectations that the Coulomb-exploded triple and double ionization processes have different degrees of orientation dependence, where the freeing of the third electron in the $Ar_2(2, 1)_{pp}$ channel is expected to be more favored when the molecule is oriented parallel to the polarization [39].

IV. CONCLUSION

In summary, we have experimentally studied the NWP dynamics in the dissociative ionization of Ar_2 induced by strong laser fields. The femtosecond pump-probe measurements in a reaction microscope allow imaging of the spatiotemporal dynamics of bound NWPs on the Ar_2^+ states. The vibrational revival and rotational excitation of the long-living rovibrational NWP were observed. The observation of time-resolved vibrational revivals enabled us to identify the three major states, i.e., $I(3/2)_u$, $II(1/2)_u$, and $I(3/2)_g$, contributing to the observed bound-state NWP motion in the Ar_2^+. Our results provide insight into the strong-field driven nuclear dynamics of vdW molecules and demonstrate the ability to precisely identify the rovibrationally excited nuclear motion in a weakly bound molecular system.

ACKNOWLEDGMENTS

This work is supported by the National Key R&D Program of China (Grant No. 2018YFA0306303) and the National Natural Science Fund (Grants No. 12304377, No. 12227807, No. 11834004, and No. 12241407).

[1] H. Niikura, F. Légaré, R. Hasbani, M. Y. Ivanov, D. Villeneuve, and P. Corkum, Probing molecular dynamics with attosecond resolution using correlated wave packet pairs, Nature (London) **421**, 826 (2003).

[2] A. H. Zewail, Laser femtochemistry, Science **242**, 1645 (1988).

[3] B. Feuerstein, T. Ergler, A. Rudenko, K. Zrost, C. Schröter, R. Moshammer, J. Ullrich, T. Niederhausen, and U. Thumm, Complete characterization of molecular dynamics in ultrashort laser fields, Phys. Rev. Lett. **99**, 153002 (2007).

[4] A. Fischer, M. Gärttner, P. Cörlin, A. Sperl, M. Schönwald, T. Mizuno, G. Sansone, A. Senftleben, J. Ullrich, B. Feuerstein, T. Pfeifer, and R. Moshammer, Molecular wave-packet dynamics on laser-controlled transition states, Phys. Rev. A **93**, 012507 (2016).

[5] F. He and U. Thumm, Dissociative ionization of H_2 in an attosecond pulse train and delayed laser pulse, Phys. Rev. A **81**, 053413 (2010).

[6] T. Ergler, A. Rudenko, B. Feuerstein, K. Zrost, C. Schröter, R. Moshammer, and J. Ullrich, Spatiotemporal imaging of ultrafast molecular motion: Collapse and revival of the D_2^+ nuclear wave packet, Phys. Rev. Lett. **97**, 193001 (2006).

[7] B. Feuerstein and U. Thumm, Mapping of coherent and decohering nuclear wave-packet dynamics in D_2^+ with ultrashort laser pulses, Phys. Rev. A **67**, 063408 (2003).

[8] M. Winter, R. Schmidt, and U. Thumm, Quantum-beat analysis of the rotational–vibrational dynamics in D_2^+, New J. Phys. **12**, 023020 (2010).

[9] I. Bocharova, A. Alnaser, U. Thumm, T. Niederhausen, D. Ray, C. L. Cocke, and I. Litvinyuk, Time-resolved Coulomb-explosion imaging of nuclear wave-packet dynamics induced in diatomic molecules by intense few-cycle laser pulses, Phys. Rev. A **83**, 013417 (2011).

[10] M. Magrakvelidze, O. Herrwerth, Y. H. Jiang, A. Rudenko, M. Kurka, L. Foucar, K. U. Kühnel, M. Kübel, N. G. Johnson, C. D. Schröter, S. Düsterer, R. Treusch, M. Lezius, I. Ben-Itzhak, R. Moshammer, J. Ullrich, M. F. Kling, and U. Thumm, Tracing nuclear-wave-packet dynamics in singly and doubly charged states of N_2 and O_2 with XUV-pump–XUV-probe experiments, Phys. Rev. A **86**, 013415 (2012).

[11] S. De, I. Bocharova, M. Magrakvelidze, D. Ray, W. Cao, B. Bergues, U. Thumm, M. F. Kling, I. Litvinyuk, and C. L. Cocke, Tracking nuclear wave-packet dynamics in molecular oxygen ions with few-cycle infrared laser pulses, Phys. Rev. A **82**, 013408 (2010).

[12] P. M. Abanador, T. Pauly, and U. Thumm, Molecular bond stabilization in the strong-field dissociation of O_2^+, Phys. Rev. A **101**, 043410 (2020).

[13] S. De, M. Magrakvelidze, I. Bocharova, D. Ray, W. Cao, I. Znakovskaya, H. Li, Z. Wang, G. Laurent, and U. Thumm, Following dynamic nuclear wave packets in N_2, O_2, and CO with few-cycle infrared pulses, Phys. Rev. A **84**, 043410 (2011).

[14] R. Johnsen and M. A. Biondi, Measurements of radiative charge-transfer reactions of doubly and singly charged rare-gas ions with rare-gas atoms at thermal energies, Phys. Rev. A **18**, 996 (1978).

[15] V. Averbukh, P. V. Demekhin, P. Kolorenč, S. Scheit, S. Stoychev, A. Kuleff, Y.-C. Chiang, K. Gokhberg, S. Kopelke, and N. Sisourat, Interatomic electronic decay processes in singly and multiply ionized clusters, J. Electron Spectrosc. Relat. Phenom. **183**, 36 (2011).

[16] U. Hergenhahn, Interatomic and intermolecular Coulombic decay: The early years, J. Electron Spectrosc. Relat. Phenom. **184**, 78 (2011).

[17] J. Qiang, I. Tutunnikov, P. Lu, K. Lin, W. Zhang, F. Sun, Y. Silberberg, Y. Prior, I. S. Averbukh, and J. Wu, Echo in a single vibrationally excited molecule, Nat. Phys. **16**, 328 (2020).

[18] N. Saito, Y. Morishita, I. Suzuki, S. Stoychev, A. Kuleff, L. Cederbaum, X.-J. Liu, H. Fukuzawa, G. Prümper, and K. Ueda, Evidence of radiative charge transfer in argon dimers, Chem. Phys. Lett. **441**, 16 (2007).

[19] C. Lu, M. Shi, S. Pan, L. Zhou, J. Qiang, P. Lu, W. Zhang, and J. Wu, Electron transfer in strong-field three-body fragmentation of $ArKr_2$ trimers, J. Chem. Phys. **158**, 094302 (2023).

[20] J. Eden, From N_2 (337 nm) to high-order harmonic generation: 40 years of coherent source development in the UV and VUV, IEEE J. Sel. Top. Quantum Electron. **6**, 1051 (2000).

[21] J. Ewing, Excimer laser technology development, IEEE J. Sel. Top. Quantum Electron. **6**, 1061 (2000).

[22] T.-K. Ha, P. Rupper, A. Wüest, and F. Merkt, The lowest electronic states of Ne_2^+, $Ar_2{}^+$ and Kr_2^+: Comparison of theory and experiment, Mol. Phys. **101**, 827 (2003).

[23] P. Rupper and F. Merkt, Dissociation energies of the I(3/2g) and I(1/2g) states of $Ar_2{}^+$, Mol. Phys. **100**, 3781 (2002).

[24] F. Naumkin, Transition intensities in rare gas triatomic ions: DIM versus point-charge approximation, Chem. Phys. **252**, 301 (2000).

[25] F. Calvo, J. Galindez, and F. Gadéa, Internal conversion in the photofragmentation of Ar_n^+ clusters ($n = 3$–8), Phys. Chem. Chem. Phys. **5**, 321 (2003).

[26] N. L. Ma, W. K. Li, and C. Ng, A Gaussian-2 *ab initio* study of van der Waals dimers R_1R_2 and their cations $R_1R_2^+$ ($R_1, R_2 =$ He, Ne, Ar, and Kr), J. Chem. Phys. **99**, 3617 (1993).

[27] P. Rupper and F. Merkt, Assignment of the first five electronic states of $Ar_2{}^+$ from the rotational fine structure of pulsed-field-ionization zero-kinetic-energy photoelectron spectra, J. Chem. Phys. **117**, 4264 (2002).

[28] W. J. Stevens, M. Gardner, A. Karo, and P. Julienne, Theoretical determination of bound–free absorption cross sections in $Ar_2{}^+$, J. Chem. Phys. **67**, 2860 (1977).

[29] F. X. Gadea and I. Paidarová, *Ab initio* calculations for $Ar_2{}^+$, He_2^+ and He_3^+, of interest for the modelling of ionic rare-gas clusters, Chem. Phys. **209**, 281 (1996).

[30] R. Mastalerz, O. Zehnder, M. Reiher, and F. Merkt, Spin–orbit coupling and potential energy functions of $Ar_2{}^+$ and Kr_2^+ by high-resolution photoelectron spectroscopy and *ab initio* quantum chemistry, J. Chem. Theory Comput. **8**, 3671 (2012).

[31] M. Magrakvelidze and U. Thumm, Dissociation dynamics of noble-gas dimers in intense two-color IR laser fields, Phys. Rev. A **88**, 013413 (2013).

[32] J. Wu, M. Magrakvelidze, A. Vredenborg, L. P. H. Schmidt, T. Jahnke, A. Czasch, R. Dörner, and U. Thumm, Steering the nuclear motion in singly ionized argon dimers with mutually detuned laser pulses, Phys. Rev. Lett. **110**, 033005 (2013).

[33] R. Dörner, V. Mergel, O. Jagutzki, L. Spielberger, J. Ullrich, R. Moshammer, and H. Schmidt-Böcking, Cold target recoil ion momentum spectroscopy: A 'momentum microscope' to view atomic collision dynamics, Phys. Rep. **330**, 95 (2000).

[34] J. Ullrich, R. Moshammer, A. Dorn, R. Dörner, L. P. H. Schmidt, and H. Schmidt-Böcking, Recoil-ion and electron momentum spectroscopy: Reaction-microscopes, Rep. Prog. Phys. **66**, 1463 (2003).

[35] W. Zhang, Z. Yu, X. Gong, J. Wang, P. Lu, H. Li, Q. Song, Q. Ji, K. Lin, J. Ma, H. Li, F. Sun, J. Qiang, H. Zeng, F. He, and J. Wu, Visualizing and steering dissociative frustrated double ionization of hydrogen molecules, Phys. Rev. Lett. **119**, 253202 (2017).

[36] W. Zhang, X. Gong, H. Li, P. Lu, F. Sun, Q. Ji, K. Lin, J. Ma, H. Li, J. Qiang, F. He, and J. Wu, Electron-nuclear correlated multiphoton-route to Rydberg fragments of molecules, Nat. Commun. **10**, 757 (2019).

[37] G. Scoles, in *Atomic and Molecular Beam Methods* (Oxford University Press, Oxford, 1988), Vol. 1, p. 14.

[38] B. Ulrich, A. Vredenborg, A. Malakzadeh, M. Meckel, K. Cole, M. Smolarski, Z. Chang, T. Jahnke, and R. Dörner, Double-ionization mechanisms of the argon dimer in intense laser fields, Phys. Rev. A **82**, 013412 (2010).

[39] J. Wu, A. Vredenborg, B. Ulrich, L. P. H. Schmidt, M. Meckel, S. Voss, H. Sann, H. Kim, T. Jahnke, and R. Dörner, Nonadiabatic alignment of van der Waals–force-bound argon dimers by femtosecond laser pulses, Phys. Rev. A **83**, 061403(R) (2011).

[40] B. Manschwetus, H. Rottke, G. Steinmeyer, L. Foucar, A. Czasch, H. Schmidt-Böcking, and W. Sandner, Mechanisms underlying strong-field double ionization of argon dimers, Phys. Rev. A **82**, 013413 (2010).

[41] J. H. Eberly, N. Narozhny, and J. Sanchez-Mondragon, Periodic spontaneous collapse and revival in a simple quantum model, Phys. Rev. Lett. **44**, 1323 (1980).

[42] J. Parker and C. Stroud, Jr., Coherence and decay of Rydberg wave packets, Phys. Rev. Lett. **56**, 716 (1986).

[43] R. W. Robinett, Quantum wave packet revivals, Phys. Rep. **392**, 1 (2004).

[44] S. Chelkowski, P. Corkum, and A. Bandrauk, Femtosecond Coulomb explosion imaging of vibrational wave functions, Phys. Rev. Lett. **82**, 3416 (1999).